HHS Public Access

Author manuscript

Sci Transl Med. Author manuscript; available in PMC 2019 September 16.

Published in final edited form as:

Sci Transl Med. 2018 January 24; 10(425): . doi:10.1126/scitranslmed.aan2742.

Miniaturized neural system for chronic, local intracerebral drug delivery

Canan Dagdeviren[1,2], **Khalil B. Ramadi**[1,3], **Pauline Joe**[1], **Kevin Spencer**[1], **Helen N. Schwerdt**[1,4], **Hideki Shimazu**[4], **Sebastien Delcasso**[4], **Ken-ichi Amemori**[4], **Carlos Nunez-Lopez**[1], **Ann M. Graybiel**[4], **Michael J. Cima**[1,5,*], **Robert Langer**[1,3,*]

[1]Koch Institute for Integrative Cancer Research, Massachusetts Institute of Technology, Cambridge, MA 02139, USA.

[2]Media Lab, Massachusetts Institute of Technology, Cambridge, MA 02139, USA.

[3]Harvard-MIT Division of Health Sciences and Technology, Massachusetts Institute of Technology, Cambridge, MA 02139, USA.

[4]McGovern Institute for Brain Research and Department of Brain and Cognitive Sciences, Massachusetts Institute of Technology, Cambridge, MA 02139, USA.

[5]Department of Materials Science, Massachusetts Institute of Technology, Cambridge, MA 02139, USA.

Abstract

Recent advances in medications for neurodegenerative disorders are expanding opportunities for improving the debilitating symptoms suffered by patients. Existing pharmacologic treatments, however, often rely on systemic drug administration, which result in broad drug distribution and consequent increased risk for toxicity. Given that many key neural circuitries have sub-cubic millimeter volumes and cell-specific characteristics, small-volume drug administration into affected brain areas with minimal diffusion and leakage is essential. We report the development of an implantable, remotely controllable, miniaturized neural drug delivery system permitting dynamic adjustment of therapy with pinpoint spatial accuracy. We demonstrate that this device can chemically modulate local neuronal activity in small (rodent) and large (nonhuman primate) animal models, while simultaneously allowing the recording of neural activity to enable feedback control.

*Corresponding author. : mjcima@mit.edu (M.J.C.); rlanger@mit.edu (R.L.).

Author contributions: C.D. designed and fabricated the MiNDS. P.J. assisted on MiNDS fabrication steps. C.D., K.B.R., A.M.G., M.J.C., and R.L. designed in vitro pump and PET studies and in vivo small- and large-animal model experiments. K.B.R., P.J., and K.S. conducted biocompatibility studies. K.B.R., C.D., P.J., K.S., and C.N.-L. designed and conducted in vitro pump characterization. K.B.R. and K.S. performed rodent surgeries, PET studies, and behavioral studies on rat models. K.S. and S.D. conducted tetrode trials on rat models. H.N.S., H.S., and K.-i.A. performed NHP surgeries and in vivo drug infusion trials in NHP. All authors discussed, analyzed, interpreted the results, and wrote and edited the manuscript.

Competing interests: C.D., M.J.C., and R.L. are inventors on a patent application (19172, 2016) submitted by MIT that covers "Systems and methods for neural drug delivery and modulation of brain activity."

Data and materials availability: The data sets, materials, and analysis generated during the current study are available from the corresponding authors on reasonable request.

SUPPLEMENTARY MATERIALS

www.sciencetranslationalmedicine.org/cgi/content/full/10/425/eaan2742/DCl

INTRODUCTION

Transformative technologies, such as functional magnetic resonance imaging (fMRI) (1), deep brain stimulation (DBS) (2), and optogenetics (3), have allowed the interrogation and manipulation of neural circuitry with increasingly high spatial and temporal resolution and show promise for therapeutic use. An emerging field is now opening to add molecular-based therapeutic systems that can deliver neurochemicals to modulate neural functions with cell-type specificity and equally high spatial and temporal targeting (4). Here, we describe a microfabricated device that fulfills this therapeutic potential by allowing the monitoring of neural circuits at a single-cell level while delivering nanodoses of therapeutic drugs to the brain.

The brain harbors many potential drug targets (*5, 6*). Many of these targets are receptors and related molecules that exist elsewhere in the body. Systemic administration of drugs will also target these peripheral receptors (7). Moreover, the brain is an exquisitely heterogeneous organ, in which tissue and cell types and functions vary on scales ranging from submillimeter to many centimeters (8). This heterogeneity can lead to an off-target exposure in the brain and to undesired effects of therapeutic agents (9). These issues have prompted attempts to deliver drugs directly to the brain using physical means (catheters). The most common delivery site is the ventricular system, which contains cerebrospinal fluid (CSF). This route can provide drug exposure to much of the brain (10), but penetrance is uneven and severely compromised by distance from the ventricular system; therefore, increasingly, drug delivery strategies are targeting specific regions of the brain (*11, 12*).

Physical targeting to small regions of the brain is challenging. The volume of exposed tissue depends on multiple parameters including concentration of the drug in the delivery medium, volume and rate of infusion, and elimination rate of the drug. Delivery volumes used to date range from 10 nl (*13,14*) to 6 ml (15). Many key neural circuit nodes have sub-cubic millimeter volumes and cell-specific identities (16). Thus, small-volume modulation in drug administration is crucial. Critically, the modulation of neural circuit dynamics requires fast, acute intervention with controllable on/off dosing to enable prompt interaction with neural network activity (17). Probes such as those used in convection-enhanced delivery, however, suffer from diffusion and leakage problems even when turned off because of the large fluidic outlet size and holdup volume within the device (18).

Because existing large-dimension neural probes can lead to significant gliosis and related deleterious tissue reaction (19), smaller probes have been developed with microfabrication techniques (*19–21*). These probes have, however, mainly been applied intracortically, penetrating only into the most superficial parts of the brain due to the designed device mechanics (low bending stiffness and small aspect ratio). A major challenge is presented by the need to access deep brain structures, centrally involved in the complex processes underlying behavior and emotion. Many studies have reported a variety of devices with various sizes, down to 70 μm (22) and infusion volumes as small as 10 nl (13). Several of these, however, serve as acute cannulae or chronic implants with an external infusion source (*14, 22–24*). A major obstacle to the clinical translation of the chronically implanted systems is the need for a versatile, implantable, closed delivery system. Previous implantable remote-

delivery systems, although valuable, are intended for use as research tools. They lack the versatility to switch out drugs or concentrations being infused or refill fluid reservoirs (*25, 26*).

Here, we report on the neuroengineering of a miniaturized neural drug delivery system (MiNDS). Key findings include the development of a MiNDS that has a diameter of 200 μm and an aspect ratio of 500. MiNDS (i) is integrated with a tungsten electrode to record neural activity for potential feedback control at the single-cell and population level, and two fluidic channels connected to modified wireless iPrecio pumps for delivering nanoliters of drugs on demand; (ii) has functioning capability over at least 2 months; and (iii) has been tested in small (rodent) and large (nonhuman primate) animal models to demonstrate chronic behavioral and acute electrophysiological effects.

RESULTS

Fabrication and design of a MiNDS

The MiNDS consists of a tungsten (W) electrode (75-μm diameter), two borosilicate (BS) channels [each with outer diameter (OD) of 30 mm and inner diameter (ID) of 20 μm], and poly(pyromellitic dianhydride-co-4,40-oxydianiline) amic acid [polyimide (PI)] templates (9.2-μm thick) that are all aligned using a vacuum tweezer inside an etched stainless steel Hamilton needle (OD = 200 μm, ID = 150 μm) (Fig. 1A and figs. S1 and S2). Stainless steel was chosen as the backbone of the MiNDS because it is mechanically robust, can be easily etched, and is compatible with chronic use in brain implants (figs. S3 to S5) (27). Furthermore, the MiNDS is scalable, with length modifiable according to the desired application (Fig. 1B). Here, the lengths of the short (S)- and long (L)-MiNDS are 1 and 10 cm, respectively. Scanning electron microscopy (SEM) imaging of the tip of a MiNDS (Fig. 1, C and D) demonstrates the BS aligner tip with a tip angle of 30° and an OD of 150 μm, consisting respectively of two 35-μm-diameter and one 80-μm-diameter openings for individual channels and an electrode. The aligner tip serves as a protective confined layer for the tip of the MiNDS and is aligned with the individual channels and electrode (Fig. 1A), capitalizing on the fact that BS is a biocompatible material in the brain (28) and can readily be etched chemically (29). A dielectric stack of silicon dioxide (SiO_2, 50 nm)/ aluminum oxide (Al_2O_3, 10 nm)/SiO_2 (50 nm) was used as an electrical insulation layer for the regions that are ~25 μm away from the electrode tip (figs. S6 and S7).

Chronic in vivo biocompatibility assessment

We performed in vivo testing using the MiNDS in a series of experiments to determine biocompatibility. The astrocytic activity measured as glial fibrillary acidic protein expression surrounding the MiNDS shank was found to be limited to ca. ~200 μm after an 8-week implantation from confocal fluorescent microscopy analyses of five rats (Fig. 1E and fig. S8, A and C). Increased microglia expression, an index of immune reaction measured as ionized calcium binding adaptor molecule 1 (Iba1), was limited to 250 μm around the MiNDS shank (fig. S8D). No neuronal degeneration was noted beyond ~50 μm from the implant as measured by NeuN staining (fig. S8E). Identical analyses near the tip of the device showed similar profile in gliosis; no neuron necrosis surrounded the tip and elevated Iba1 expression

for 450 μm around the implant (fig. S8, F to H). Together, these results show that 8 weeks after implantation of the MiNDS, cell death and immune activation is limited to the tissue surrounding the implant.

iPrecio SMP-300 pump in vitro infusion characterization

We next connected the MiNDS into two independently controlled, modified, SMP-300 iPrecio pumps (Fig. 2A and fig. S9) and used a precision microbalance to determine the in vitro behavior of the system (Fig. 2B and fig. S10). Modifications to the pump to improve the accuracy of drug delivery involve replacing the original high-compliance thermoplastic infusion tubing (elastic modulus, 1 to 200 MPa) with high-pressure, low-compliance polyether ether ketone (PEEK) tubing with an elastic modulus of 3.6 GPa and using stainless steel adapters. The iPrecio pumps allow for refilling of the reservoir even while implanted via a septum that can be penetrated using a 31-gauge needle. The peristaltic pistons separate reservoir pressure from the fluid in the cannula, preventing accidental leakage. The infused medium used for in vitro infusion characterizations was deionized (DI) water. The average infusion profile of the L- and S-MiNDS system was measured for 10 min at the flow rates of 10, 1, and 0.1 μl/hour (Fig. 2C and fig. S11, A to C). Longer infusion profiles at a different flow rate (6 μl/hour for 20 min) through S- and L-MiNDS were also measured (fig. S11D). The system performed with 3.3% accuracy at the rate of 10 μl/hour infusion (Fig. 2C). Comparisons with unmodified iPrecio pumps were performed with two infusion profiles (1 and 10 μl/hour for 10 min) (fig. S11, E to F). These comparisons show the significant compliance buildup in unmodified pumps, as evidenced by most of the fluid being output past the end of infusion. No infusion past the programmed end of pumping was noted in modified pumps, indicating that the compliance of the system is negligible and that there is a negligible passive leakage of fluid out of the BS channel. The flow rates of MiNDS are one order of magnitude lower than those used in convection-enhanced delivery (30). These results show that the MiNDS can be acutely turned on or off to provide a controlled fluid release without causing noticeable leaking, therefore suggesting that the use of MiNDS might be an effective strategy to achieve repeated local drug delivery in small deep brain regions.

Infusion characterization of the MiNDS via PET

We confirmed the system functionality of the MiNDS device in the rat brain using three-dimensional positron emission tomography (PET) imaging to visualize and characterize in vivo deep brain infusions (31). A 0.6% (by weight) agarose solution with an embedded S-MiNDS was used as a representative homogeneous brain phantom to perform the control trials. For the in vivo testing, an S-MiNDS targeting the substantia nigra (SN), a brain region containing dopaminergic neurons, was chronically implanted in a rat. To validate the tunable infusion capability of the MiNDS, large (1.67 μl over 10 min) and small (667 nl over 4 min) infusions of copper-64 (Cu-64), a positron-emitting isotope regularly used for PET imaging (32), were performed. Accounting for the internal volume of the device, these infusions resulted in a 1.2-μl and 167-nl net volume delivered to the brain, respectively. A syringe pump was used to deliver infusions in the agarose control and in vivo, whereas iPrecio pumps were used only in vivo. The large infusion (1.67 μl) into the agarose control with a syringe pump produced a bolus with a volume of $3.78 \pm 2.43\ mm^3$ (fig. S12, A, D, and E).

An identical large-volume infusion delivered by a syringe pump in vivo produced a bolus volume of 4.64 ± 1.43 mm^3 (fig. S12, B, D, and F); the in vivo iPrecio infusion resulted in a bolus with a volume of 4.36 ± 0.45 mm^3 (Fig. 2, D to F, and fig. S12, C, D, G, and H). Identical studies done with the smaller infusion (667 nl) formed a bolus volume of 2.35 ± 1.14 mm^3 in the agarose brain phantom (fig. S13, A, D, E, and F) and volume of 1.81 ± 0.00 mm^3 and 2.80 ± 0.15 mm^3 in vivo using the syringe and iPrecio pumps, respectively (fig. S13, B to E and G to I). We observed localized bolus delivery in all cases, with ~1-mm diffusion in each direction for the largest volume infusions (Fig. 2E). These results demonstrate the capability of the MiNDS to control the delivery of small quantities of the drug remotely into a rat brain area without any tethering or physical connection. The time sequence of PET images acquired at various time points further show the capability of the MiNDS to maintain a localized bolus delivery (figs. S12 and S13). The collective infusion results indicate that MiNDS avoids the problems of backflow that we encountered in acute infusions (removing the needle after drug delivery) (fig. S14) and can deliver nano-liter quantities of drugs in a tunable, repeatable manner. In addition, no delay in infusion was noted, suggesting that no effective resistance to infusion developed up to 65 days after implantation (fig. S15). This confirms that MiNDS retains chronic functionality in vivo up to 8 weeks.

In vivo evaluation of the MiNDS in anesthetized rats

We next performed acute electrophysiological recordings and micro-injections in anesthetized rats ($n = 2$) to test the MiNDS with a tetrode (T-1, T-2, T-3, T-4) tungsten electrode (Fig. 3, A to C, and fig. S16). We measured the firing rate of a single neuron after infusion of control solution (saline, 100 nl/min for 3 min) and muscimol, a γ-aminobutyric acid agonist known to reduce neuronal firing (100 nl/min for 3 min), in the rat hippocampus. There was a smaller than 10% change in firing rate after the saline infusion (12.8 spikes/s before, 11.6 spikes/s after) and after one muscimol infusion (11.6 spikes/s before, 10.6 spikes/s after). Therefore, we performed a second muscimol infusion, which completely abolished neuronal firing (Fig. 3, A to C, and table S1). The amplitude of the action potentials recorded simultaneously from different tungsten wires of the same tetrode electrode (T1 and T2; Fig. 3B) is used to isolate signals coming from different neurons (33). The stability of the recorded neurons during multiple injections did not affect the shape of their action potentials (Fig. 3C). The ability of MiNDS to deliver muscimol and consequently inhibit neuronal activity was confirmed in a second neuron in a different animal (fig. S17A and table S1). The mean normalized spike rate for each infusion intervals for both trials is shown in fig. S17B. We also implanted a MiNDS in the striatum of another rat and recorded local field potentials (LFPs) for up to 4 weeks (fig. S18A). Spectral analysis of LFPs reveals robust and consistent θ-band activity up to 4 weeks after implantation (fig. S18, B and C), indicating the ability of MiNDS to record neuronal activity in anesthetized rats while chronically implanted.

In vivo behavioral evaluation of the MiNDS in awake rats

We tested the capability of interfacing the MiNDS with deep brain structures to remotely control behavior. S-MiNDS was implanted in the rat SN and connected to two implanted iPrecio pumps, containing either saline or muscimol (Fig. 3, D and E, and figs. S19 and

S20). Unilateral delivery of muscimol to the SN is known to evoke preferential ipsilateral rotation of the animal, reflecting a hemiparkinsonian state (34). This parkinsonian behavior was induced by remotely controlled infusion of 1.67 μl of muscimol (0.2 mg/ml) through the MiNDS but not by comparable injection of saline (Fig. 3, F to H). Muscimol remained stable up to 50 days at 37°C (fig. S21). Muscimol infusion induced a 52-fold increase in the number of clockwise (CW) rotations without affecting counterclockwise (CCW) rotations (n = 3 rats, three trials per rat, $*P < 0.01$; Fig. 3H and fig. S22). These experiments illustrate the ability of MiNDS to repeatedly and reproducibly deliver small volumes of drugs that can induce behavioral changes.

In vivo evaluation of the MiNDS in a rhesus macaque monkey

We further confirmed the functionality of the MiNDS (specifically, the L-MiNDS) in a large animal model, the rhesus macaque (*Macaca mulatta*) monkey (Fig. 4, A and B). The L-MiNDS was used to modulate and monitor local neuronal activity in the neocortex of a head-fixed monkey through serial infusions of artificial CSF (aCSF) and muscimol (Fig. 4C). The impedance measurement of the tungsten electrode was 1.5 MΩ in brain and 2 MΩ at preimplantation in saline. Modulation of neuronal firing activity was monitored by recording signals at the MiNDS electrode adjoining the infusion ports. The MiNDS was lowered until stable recording of a unit was observed to establish a baseline for comparison of firing rates and unit waveforms. Then, aCSF was infused for 5 min and 20 s at an infusion rate of 100 nl/min. This control infusion reduced the firing rate by 33.2% compared to preinfusion baseline (2.0 spikes/s before, 1.3 spikes/s after; $P < 0.0001$) without affecting unit waveform during and after the infusion (Fig. 4C). Muscimol was then infused at the same location for 5 min at an infusion rate of 100 nl/min. This infusion decreased the rate of detected spike activity by 97% as compared with the period between the aCSF infusion and the muscimol infusion (1.3 spikes/s before, 0.04 spikes/s after; $P < 0.0001$) (Fig. 4C). The average spike waveforms were highly correlated between periods (Fig. 4D and fig. S23; Pearson's correlation coefficient, $R = 0.96$ for average waveforms between baseline and post-aCSF, and $R = 0.92$ for average waveforms between post-aCSF and post-muscimol) suggesting that the same unit was being monitored throughout the serial infusion experiments.

A second experiment was conducted to target deeper layers of the neocortical region (dorsal bank of the cingulate cortex) (35). We asked whether we could reverse the effect of muscimol on neuronal firing through an additional infusion of aCSF at this adjoining site. Our results show that infusion of aCSF was effective in reversing the inhibitory effect of muscimol (fig. S24, A to C), with waveforms closely resembling those found during the pre-muscimol period (fig. S24, D to G). We replicated the results of the first experiment through an aCSF control infusion, which minimally changed the firing rate (0.5 spikes/s before, 0.6 spikes/s after), and subsequent muscimol infusion, which decreased the firing rate (0.6 spikes/s, 0.08 spikes/s after) (fig. S24). A summary of all statistical calculations is given in table S1. We further evaluated LFP activity changes induced by the infusions. Broadband power from 30 to 100 Hz remains relatively consistent from baseline (–10 min) to post-aCSF infusion periods (0, 10, and 20 min) and decreases immediately after muscimol infusion (30 min, and all subsequent periods) (fig. S25A). α-band (7 to 13 Hz) and β-band

(13 to 30 Hz) power fluctuate without correlation to the infusions (fig. S25B). The prominent power at 60 Hz is due to coupling of power mains noise (fig. S25A). Relative baseline power is demarcated with a horizontal dashed black line across both plots to show relative changes in LFP broadband power that is especially visualized in fig. S25A 20 min after muscimol infusion (black arrow). Collective results in the NHP demonstrated the fine, localized, bidirectional control capabilities of the MiNDS.

DISCUSSION

Chronically implanted neural probes provide the ability to modulate specific brain regions for therapy (2). This study presents a miniaturized neural drug delivery system called MiNDS as a versatile platform for multimodal interfacing in small and large animals. We show here that MiNDS can chemically modulate the local neuronal activity and related behavior in animal models while simultaneously recording neuronal electroencephalogram (EEG) activity.

We demonstrated that MiNDS was able to deliver drugs selectively in small deep brain structures in a controlled manner in rats and in a monkey. Moreover, longitudinal analysis in rodents shows that MiNDS performances were stable for up to 2 months in vivo, suggesting that the platform might be used for chronic treatment and recording.

We conducted series of trials in small (rodent) and large (NHP) animal models demonstrating chronic behavioral and acute electrophysiological effects, respectively. By inducing a reversible hemiparkinsonian state in rats, we illustrated the ability of MiNDS to interface with deep brain circuitry. Many neurological disorders, such as Parkinson's disease, arise due to dysfunctional basal ganglia circuits. The ability, then, to modulate this circuitry suggests the potential to use implanted MiNDS as therapy for such disorders.

The possibility to perform serial infusions of multiple distinct drugs while simultaneously recording the local EEG activity will be important for clinical applications that may require a chronic recording from a fixed brain location (36) and an online analysis to detect changes in LFP activity caused by drug delivery in real time. For example, pathological β-band LFP oscillations in Parkinson's disease and/or epileptic discharges in epilepsy could be recorded from the chronically integrated electrode to track and treat dysfunctions with multidrug therapies.

Together, these experiments demonstrate that this miniaturized, customizable device with high-bending stiffness, high aspect ratio, and adjustable number of stainless steel channels can reliably reach deep brain structures in small- and large-animal models without the need of an extraneous guide tube to implant.

Current therapies for neurological disorders remain limited. New tools are needed to treat the most severe cases of neuropsychiatric disorders (*19*–*21*). The capacity to selectively deliver drugs on demand to brain structures could greatly improve the therapeutic outcome and minimize unwanted side effects over currently available methods (4). The results shown here motivate future research efforts to facilitate the incorporation of MiNDS technologies in neural drug development and therapy. We note that in addition to treating neurological

disorders, the customizable feature of this microfabricated device could open new routes to deliver chemicals, light, and electricity to other organs with pinpoint spatiotemporal resolution. Optogenetics of peripheral nerves together with electrical and chemical interfacing could be achieved through a single implant (37). Another potential use of MiNDS could be to achieve the targeted delivery of chemo-therapeutics to tumors in the body. Such a technique would enable delivery of higher doses without associated systemic toxicity (38). MiNDS could also be used to deliver growth factors and stem cells to regions of significant cellular necrosis (39). For neurological and cardiovascular diseases, combining growth factor therapy with electrical stimuli might help regenerate electroactive cells.

A number of improvements can be incorporated to MiNDS to enhance clinical translation. Substituting device components with nonmetallic materials would offer MRI compatibility. Thin hydrogel coatings along the device shaft could further enhance biocompatibility (40). The short life span of the current pump batteries is a limitation for chronic use. For use beyond 1 month, batteries would have to be changed frequently, requiring recurring surgical procedures with associated complication risks and additional health care costs. One promising solution is to use energy harvesting through natural organ movement to recharge or replace batteries (41). Other improvements to this technology may include sensors at the tip of MiNDS to monitor real-time phenotypic parameters such as temperature, pressure, stiffness during drug infusions, and an integrated tissue retrieval channel for obtaining brain biopsies. Such multi-modal capabilities would allow for more in-depth investigation into the pathology of neurological conditions in vivo. Incorporating these sensors would also permit closed-loop therapy of neurological disorders (42). Closed-loop electrical stimulation has been shown to be superior to blind DBS for the treatment of epilepsy (43) and Parkinson's diseases (44). These developments could pave the way toward an adaptive, multimodal treatment for neurologic disease and eventually revolutionize therapy for patients.

MATERIALS AND METHODS

Study design

The objectives of the studies were to develop a biocompatible, remotely controllable, MiNDS that permits dynamic neural adjustment with pinpoint spatial resolution in small- and large-animal models. We first characterized the performance of the system in vitro, using an ultrahigh-precision microbalance to detect nanoliter infusions. We performed in vivo acute electrophysiological recordings and micro-injections in anesthetized rats. Next, we tested the capability of interfacing the MiNDS with deep brain structures to remotely control behavior in the rat SN. We further confirmed the functionality of the MiNDS in a large, awake behaving animal model, the rhesus macaque *(Macaca mulatta)* monkey. We characterized the tissue reaction to the chronic MiNDS implant using immunohistochemical staining for neural cell markers. Sample sizes were chosen to demonstrate statistical significance. Tissue sections were scored by a MATLAB image analysis algorithm, and behavioral data were analyzed using EthoVision software in a blinded manner. Mean values and SDs are indicated in each figure legend.

Fabricating the polymer template

A silicon (Si) wafer was coated with a 50-nm-thick layer of poly(methyl methacrylate) (PMMA 495 A2) at 3000 rpm (Headway Research, PWM32) for 30 s and baked on a hotplate at 180°C for 2 min. A poly(pyromellitic dianhydride-co-4,40-oxydianiline) amic acid solution was then spun at 4000 rpm for 30 s and precured on a hotplate at 150°C for 1 min to form a 1.3-μm-thick PI layer (*45–47*). This step was repeated for seven times to reach a ~9.2-μm-thick layer of PI. Next, the sample was cured in a vacuum oven at 250°C for 1 hour. The walls of the PI template (depth of 2.8 μm) were formed by reactive ion etching (March RIE, Nordson) through a pattern of photoresist (AZ 4620, Clariant) until the layer of PMMA was reached on the Si wafer (fig. S1). The length of the PI template is set to 7 cm.

Customizing the stainless steel needle for the MiNDS

The OD of a stainless steel needle (30-gauge, Hamilton Company) (fig. S2) was etched down to 200 mm via a chemical solution of 10 wt % (weight %) ferric chloride ($FeCl_3$), 10 wt % hydrochloric acid (HCl), and 5 wt % nitric acid (HNO3) at 50°C with an etching rate of 2 μm/min (48). To protect the inner wall of the stainless steel needle from the chemical solution, a PI tubing was tightly placed inside and then removed after the etching process (figs. S1 and S2).

Polishing the tip of the BS channel to a 30° angle

A BS channel with an ID of 20 μm and an OD of 80 mm (VitroCom Inc.) was firstly etched down to 30 μm via a chemical solution of hydro-fluoric acid (HF 48%, Sigma-Aldrich) in DI water (volume ratio of 1:2) with an etching rate of 6 μm/min. The ends of the BS channel were protected via three layers of PI tape (Caplinq Corporation, 20-μm thick). Afterward, the BS was placed into the polisher holder, angled to 30°, and positioned until the tip touched the polishing film (20.3-cm-diameter aluminum oxide, Al_2O_3, polishing film, ULTRA TEC Manufacturing Inc.). The lap speed was set to 250 rpm. After the tip of the BS channel was polished for ~2 hours, it was immersed into water in an ultrasonic cleaner (KENDAL, model CD-3800A) for ~3 min to clean the remaining residues (figs. S3 and S4).

Electrical insulation of the tungsten electrodes

A dielectric stack of silicon dioxide (SiO_2) (50 nm)/aluminum oxide (Al_2O_3) (10 nm)/SiO_2 (50 nm) was deposited on the tungsten electrode (FHC Inc.) via plasma-enhanced chemical vapor deposition (PlasmaTherm System VII) and atomic layer deposition (Cambridge NanoTech Inc.), respectively, to provide electrical insulation. The exposed tungsten electrode tip (~9700 μm^2) was defined by dipping the wire into polyvinyl alcohol (PVA) solution with a depth of ~25 μm (fig. S5). After the dielectric stack deposition, the protective layer of PVA on the tungsten tip was dissolved in a water bath.

Aligning the channels on the PI template and assembling the MiNDS

A 2-cm-thick stamp of polydimethylsiloxane (Sylgard 184), with a length and a width of 8 and 2 cm, respectively, and a mixing ratio of 8.5:1.5 base to cross-linker, was used to pick up the BS channels and the electrode gently and aligned it with the PI template under optical microscopy with the help of a mask aligner (Karl Suss Model MA4) (fig. S1, H and I). Two

BS channels were then aligned side by side on the PI template, whereas the electrode was placed on the center of the glass tubes. A ~3-μm-thick layer of ultraviolet (UV) light-curable silicone adhesive (UV epoxy, LOCTITE 5055, Henkel Corp.) coated the PI template and covered both the channels and the electrode inside a desiccator. Once the epoxy was cured, the PI template with the channels and the electrode was immersed in a hot (85°C) acetone bath to allow the sacrificial layer of PMMA to dissolve away (fig. S1J). The epoxy-coated PI template was then physically free and could be retrieved from the acetone bath. Afterward, the PI was aligned with the polished end of the needle hole and aligned along the needle hole by using a vacuum tweezer (Ted Pella Inc., Vacuum Pickup System, 115 V), which holds the template gently from the other end with a vacuum of 50.8 cm of mercury.

A customized BS tip aligner (VitroCom Inc.) was obtained containing two 35-μm-diameter and one 90-μm-diameter channels to serve as the alignment of the fluidics and the electrode, respectively. The tip of the tip aligner was also polished to an angle of 30° (fig. S6). The length of the aligner tip can be engineered, and the other end was polished with an angle of 0°. Later, the blunt end of the aligner tip was aligned with the expanded electrode and attached to the precured epoxy layer in the tip of the needle. The fluidic connections to connect the channels to the wireless pumps were created via PEEK tubes (Tub Radel R, IDEX Health & Science LLC, 1.59 mm OD × 0.25 mm ID) and followed by UV-epoxy sealing.

The fluidic connection is simply made by aligning the PEEK tubing with flexible BS channels in the metal cup of stainless steel needle under microscope and filling all the gaps with UV epoxy with a connection yield of ~100%. The electrical connection to the electrode was made via a metal pin (Conn Recept Pin, Mill-Max Manufacturing Corp, 7.62 mm length, ~0.38 mm to ~0.56 mm accepting pin diameter, 0.94 mm mounting hole diameter, 0.79 mm pin hole diameter, 1.04 mm flange diameter, 0.46 mm tail diameter, 3.81 mm socket depth). The UV epoxy was then used to fill the gap between the PI template and the needle hole via vacuum tube, sucking from one end and filling with epoxy on the other end of the needle. Because the MiNDS is scalable, its length can be modified according to the desired subject application (figs. S7 and S8).

Chronic in vivo biocompatibility assessment

Four rats underwent the MiNDS implantation as described in the rat surgery section. At 56 days after implantation, the animals were euthanized using carbon dioxide asphyxiation. Each animal consequently underwent cardiac perfusion of 60 ml of 1× phosphate-buffered saline solution (Corning Inc., Corning), followed by 60 ml of 4% paraformaldehyde (PFA) solution (Alfa Aesar). The head was then removed and immersed in 4% PFA for 48 hours. The implanted devices were extracted, and the brain was removed and placed in 4% PFA overnight and subsequently in sinking solutions of increasing sucrose (AMRESCO Inc.) concentration (10, 20, and 30% w/v) overnight or until the brain sinked (Fig. 1). All animal protocols were approved by the Massachusetts Institute of Technology (MIT) Committee for Animal Care (0714–072-17).

iPrecio SMP-300 pump in vitro infusion characterization

To achieve fine control over volume delivery, it was necessary to add modifications to the pump, such as replacing the original high-compliance thermoplastic infusion tubing (elastic modulus, 1 to 200 MPa) with high-pressure, low-compliance PEEK tubing (elastic modulus, 3.6 GPa) and stainless steel adapters. For each of the two iPrecio SMP-300 pumps (Primetech Corp.) used, the original external tubing was cut, leaving only the first 2.5 mm of outlet tubing (fig. S12, A and B). A 24-gauge stainless steel connector was inserted into the pump fluid outlet, and a 31-gauge connector was placed within the larger connector (fig. S12C). The two steel connectors are glued together using UV epoxy, creating a water-tight secure junction (fig. S12, D and E). The protruding end of the 31-gauge connector was inserted into the PEEK tubing of the MiNDS, and the junction was again glued with UV epoxy (fig. S12F). The MiNDS was placed into a custom-made polytetrafluoroethylene holder (manufactured with CNC Micro Machining Center-S, Cameron Microdrill Presses) and attached to a syringe pump to be used as a vertical frame (Harvard Apparatus PHD 2000) (fig. S12, G and H). The assembly was combined with a computer-controllable Mettler Toledo microbalance for pump characterization experiments (fig. S12J).

A plastic weighing dish was made by cutting the needle cap of a 28-gauge blunt needle using a stainless steel blade (fig. S13). The dish was half-filled with DI water (~30 ml) and placed on the weighing plate of the microbalance (fig. S13, F to H). The glass cap of the microbalance was removed, and parafilm was stretched over the top (fig. S13C). A circular hole was cut out in the center of the parafilm using scissors (fig. S13, D and E). The MiNDS was lowered through the hole, and the pump set was used to infuse fluid until a drop of fluid appears at the top of the MiNDS (fig. S13, I and J). At this point, the device was lowered further down until the tip of the MiNDS was submerged in the water of the weighing dish. To minimize water evaporation, we placed a 20-ml mineral oil layer (paraffin oil and liquid petrolatum, Mallinckrodt Chemicals) on top of the water of the weighing dish (fig. S13L). The system was allowed to stabilize before any infusions were tested. The pump was programmed wirelessly using proprietary iPrecio pump software (more information can be found at: http://iprecio.com/products/tabid/212/Default.aspx).

The microbalance was set to read output twice per second and send the data to a computer via a RS232 serial connector. Commercially available Advanced Serial Data Logger software (AGG Software) was used to acquire the data and export it to Microsoft Excel for further analysis. For every infusion, data recording begins and ends at least 10 min before and after infusion onset and end, respectively. This process was repeated for both L- and S-MiNDS, and each infusion protocol was run for four times. The four infusion protocols were run for each device: (i) 10 μl/hour for 10 min, (ii) 1 μl/hour for 10 min, (iii) 0.1 μl/hour for 10 min, and (iv) 6 ml/hour for 20 min.

Statistical analysis

We performed χ^2 tests in NHP and rodent tetrode trials to calculate significant differences in spike firing rate before and after infusion of aCSF and muscimol (Fig. 4, fig. S24, and table S1). We used Pearson's correlation coefficient (R) to evaluate the similarity between waveforms (Fig. 4). The mean waveform for each period in Fig. 4 was computed to calculate

R between periods: 4593 waveforms in base-line period (25 min), 51 waveforms in post-aCSF period (20 min), and 165 waveforms in post-muscimol period (46 min). Averaged action potentials of a well-isolated unit (single unit) are given in Fig. 3C during each period (saline infusion, 20,940 waveforms; muscimol 1 infusion, 19,073 waveforms; and muscimol 2 infusion, 132 waveforms; $n = 1$ unit). Orange shading represents a band around the mean with a width of three SDs. Immunohistochemical slides were imaged with fluorescent microscopy and analyzed using MATLAB. Fluorescence intensity was quantified in 2-μm radial increments away from the implant site, up to 1100 μm away. We performed one-way analysis of variance (ANOVA) with Dunnett's post hoc test to calculate significant differences in fluorescence intensity near the implant compared to far field ($*P < 0.05$, $**P < 0.01$, $***P < 0.005$, and $****P < 0.001$). PET data were analyzed by calculating the sum intensity at the infusion site region of interest. This was done for three scenarios: syringe pump infusion into agarose, syringe pump into brain, and iPrecio pump into brain. One-way ANOVA with Tukey post hoc test was used to determine the significant difference in the intensity between scenarios at each time point ($*P < 0.0332$ and $***P < 0.0002$). Behavioral modulation in rodents was assessed by comparing the number of CW and CCW rotations made (i) before saline infusion, (ii) post-saline infusion, and (iii) post-muscimol infusion. One-way ANOVA with Tukey post hoc test was performed to calculate significant differences among number of CW rotations in each trial period, as well as CCW rotations in each period ($***P < 0.0001$).

Supplementary Material

Refer to Web version on PubMed Central for supplementary material.

Acknowledgments:

We thank P. Bhagchandani and Z. Wei for technical support during device fabrication and S. C. Dagdeviren for the useful suggestions in device design. We acknowledge the cleanroom facilities of Harvard University Center for Nanoscale Systems and MIT Microsystems Technology Laboratories. We thank H. Mak and the Animal Imaging Core Facility at the Koch Institute for Integrative Cancer Research for help with PET imaging and the facility access, respectively.

Funding: This study was supported by the NIH, National Institute of Biomedical Imaging and Bioengineering (R01 EB016101 to R.L., A.M.G., and M.J.C.).

REFERENCES AND NOTES

1. Glover GH, Overview of functional magnetic resonance imaging. Neurosurg. Clin. N. Am. 22, 133–139 (2011). [PubMed: 21435566]
2. Perlmutter JS, Mink JW, Deep brain stimulation. Annu. Rev. Neurosci. 29, 229–257 (2006). [PubMed: 16776585]
3. Deisseroth K, Optogenetics. Nat. Methods 8, 26–29 (2011). [PubMed: 21191368]
4. Stuber GD, Mason AO, Integrating optogenetic and pharmacological approaches to study neural circuit function: Current applications and future directions. Pharmacol. Rev. 65, 156–170 (2013). [PubMed: 23319548]
5. Soilu-Hänninen M, Epa R, Shipham K, Butzkueven H, Bucci T, Barrett G, Bartlett PF, Kilpatrick TJ, Treatment of experimental autoimmune encephalomyelitis with antisense oligonucleotides against the low affinity neurotrophin receptor. J. Neurosci. Res. 59, 712–721 (2000). [PubMed: 10700008]

6. Erickson MA, Niehoff ML, Farr SA, Morley JE, Dillman LA, Lynch KM, Banks WA, Peripheral administration of antisense oligonucleotides targeting the amyloid-β protein precursor reverses AβPP and LRP-1 overexpression in the aged SAMP8 mouse brain. J. Alzheimer's Dis. 28, 951–960 (2012). [PubMed: 22179572]
7. Ricci A, Mignini F, Tomassoni D, Amenta F, Dopamine receptor subtypes in the human pulmonary arterial tree. Auton. Autacoid Pharmacol. 26, 361–369 (2006). [PubMed: 16968475]
8. Corbetta M, Shulman GL, Control of goal-directed and stimulus-driven attention in the brain. Nat. Rev. Neurosci. 3, 201–215 (2002). [PubMed: 11994752]
9. Pardridge WM, Drug transport in brain via the cerebrospianl fluid. Fluids Barriers CNS 8, 7 (2011). [PubMed: 21349155]
10. Blasberg RG, Patlak C, Fenstermacher JD, Intrathecal chemotherapy: Brain tissue profiles after ventriculocisternal perfusion. J. Pharmacol. Exp. Ther. 195, 73–83 (1975). [PubMed: 810575]
11. Asthana S, Gupta PK, Chaurasia M, Dube A, Chourasia MK, Polymeric colloidal particulate systems: Intelligent tools for intracellular targeting of antileishmanial cargos. Expert Opin. Drug Deliv. 10, 1633–1651 (2013). [PubMed: 24147603]
12. Blakeley J, Drug delivery to brain tumors. Curr. Neurol. Neurosci. Rep. 8, 235–241 (2008). [PubMed: 18541119]
13. Parada MA, de Parada Puig M., Hoebel BG, A new triple-channel swivel for fluid delivery in the range of intracranial (10 nl) and intravenous (100 μl) self-administration volumes and also suitable for microdialysis. J. Neurosci. Methods 54, 1–8 (1994). [PubMed: 7815813]
14. Ikemoto S, Sharpe LG, A head-attachable device for injecting nanoliter volumes of drug solutions into brain sites of freely moving rats. J. Neurosci. Methods 110, 135–140 (2001). [PubMed: 11564533]
15. Lewis O, Woolley M, Johnson D, Rosser A, Barua NU, Bienemann AS, Gill SS, Evans S, Chronic, intermittent convection-enhanced delivery devices. J. Neurosci. Methods 259, 47–56 (2016). [PubMed: 26617320]
16. Trost M, Su S, Su P, Yen RF, Tseng HM, Barnes A, Ma Y, Eidelberg D, Network modulation by the subthalamic nucleus in the treatment of Parkinson's disease. Neuroimage 31, 301–307 (2006). [PubMed: 16466936]
17. Patchell RA, Regine WF, Ashton P, Tibbs PA, Wilson D, Shappley D, Young B, A phase I trial of continuously infused intratumoral bleomycin for the treatment of recurrent glioblastoma multiforme. J. Neurooncol 60, 37–42 (2002). [PubMed: 12416544]
18. Varenika V, Dickinson P, Bringas J, LeCouteur R, Higgins R, Park J, Fiandaca M, Berger M, Sampson J, Bankiewicz K, Detection of infusate leakage in the brain using real-time imaging of convection-enhanced delivery. J. Neurosurg. 109, 874–880 (2008). [PubMed: 18976077]
19. De Faveri S, Maggiolini E, Miele E, De Angelis F, Cesca F, Benfenati F, Fadiga L, Bio-inspired hybrid microelectrodes: A hybrid solution to improve long-term performance of chronic intracortical implants. Front. Neuroeng. 7, 7 (2014). [PubMed: 24782757]
20. Takeuchi S, Ziegler D, Yoshida Y, Mabuchi K, Suzuki T, Parylene flexible neural probes integrated with microfluidic channels. Lab Chip 5, 519–523 (2005). [PubMed: 15856088]
21. Gao K, Li G, Lia L, Cheng J, Zhao J, Xu Y, Fabrication of flexible microelectrode arrays integrated with microfluidic channels for stable neural interfaces. Sens. Actuators A 197, 9–14 (2013).
22. Lee HJ, Son Y, Kim D, Kim YK, Choi N, Yoon E-S, Cho I-J, A new thin silicon microneedle with an embedded microchannel for deep brain drug infusion. Sens. Actuators B 209, 413–422 (2015).
23. Altuna A, Bellistri E, Cid E, Aivar P, Gal B, Berganzo J, Gabriel G, Guimera A, Villa R, Fernández LJ, Menendez L de la Prida, SU-8 based microprobes for simultaneous neural depth recording and drug delivery in the brain. Lab Chip 13, 1422–1430 (2013). [PubMed: 23407672]
24. Rohatgi P, Langhals NB, Kipke DR, Patil PG, In vivo performance of a microelectrode neural probe with intergrated drug delivery. Neurosurg. Focus 27, E8 (2009).
25. Jeong J-W, McCall JG, Shin G, Zhang Y, Al-Hasani R, Kim M, Li S, Sim JY, Jang K-J, Shi Y, Hong DY, Liu Y, Schmitz GP, Xia L, He Z, Gamble P, Ray WZ, Huang Y, Bruchas MR, Rogers JA, Wireless optofluidic systems for programmable in vivo pharmacology and optogenetics. Cell 162, 662–674 (2015). [PubMed: 26189679]

26. Spieth S, Schumacher A, Messner S, Zengerle R, The NeuroMedicator—A micropump integrated with silicon microprobes for drug delivery in neural research. J. Micromech. Microeng. 22, 065020 (2012).
27. Mofid MM, Thompson RC, Pardo CA, Manson PN, Kolk Vander C. A., Biocompatibility of fixation materials in the brain. Plast. Reconstr. Surg. 100, 14–20 (1997). [PubMed: 9207654]
28. Parthasarathy KS, Cheng YC, McAllister JP II, Shen Y, Li J, Deren K, Haacke EM, Auner W, Biocompatibilities of sapphire and borosilicate glass as cortical neuroprostheses. Magn. Reson. Imaging 25, 1333–1340 (2007). [PubMed: 17462843]
29. Blass J, Köhler O, Fingerle M, Müller C, Ziegler C, Properties and characteristics of wet (HF) and dry (RIE) etched borosilicate glass. Phys. Status Solidi A 210, 988–993 (2013).
30. Lonser RR, Sarntinoranont M, Morrison PF, Oldfield EH, Convection-enhanced delivery to the central nervous system. J. Neurosurg. 122, 697–706 (2015). [PubMed: 25397365]
31. Haar PJ, Stewart JE, Gillies GT, Prabhu SS, Broaddus WC, Quantitative three-dimensional analysis and diffusion modeling of oligonucleotide concentrations after direct intraparenchymal brain infusion. IEEE Trans. Biomed. Eng. 48, 560–569 (2001). [PubMed: 11341530]
32. Anderson CJ, Ferdani R, Copper-64 radiopharmaceuticals for PET imaging of cancer: Advances in preclinical and clinical research. Cancer Biother. Radiopharm. 24, 379–393 (2009). [PubMed: 19694573]
33. Gray CM, Maldonado PE, Wilson M, McNaughton B, Tetrodes markedly improve the reliability and yield of multiple single-unit isolation from multi-unit recordings in cat striate cortex. J. Neurosci. Methods 63, 43–54 (1995). [PubMed: 8788047]
34. Martin GE, Papp NL, Bacino CB, Contralateral turning evoked by the intranigral microinjection of muscimol and other GABA agonists. Brain Res. 155, 297–312 (1978). [PubMed: 567515]
35. Rauch SL, Jenike MA, Alpert NM, Baer L, Breiter HCR, Savage CR, Fischman AJ, Regional cerebral blood flow measured during symptom provocation in obsessive- compulsive disorder using oxygen 15—Labeled carbon dioxide and positron emission tomography. Arch. Gen. Psychiatry 51, 62–70 (1994). [PubMed: 8279930]
36. Little S, Pogosyan A, Neal S, Zavala B, Zrinzo L, Hariz M, Foltynie T, Limousin P, Ashkan K, Fitzgerald J, Green AL, Aziz TZ, Brown P, Adaptive deep brain stimulation in advanced Parkinson disease. Ann. Neurol. 74, 449–457 (2013). [PubMed: 23852650]
37. Montgomery KL, Yeh AJ, Ho JS, Tsao V, Iyer SM, Grosenick L, Ferenczi EA, Tanabe Y, Deisseroth K, Delp SL, Poon ASY, Wirelessly powered, fully internal optogenetics for brain, spinal and peripheral circuits in mice. Nat. Methods 12, 969–974 (2015). [PubMed: 26280330]
38. Hurria A, Mohile S, Gajra A, Klepin H, Muss H, Chapman A, Feng T, Smith D, Sun C-L, Glas ND, Cohen HJ, Katheria V, Doan C, Zavala L, Levi A, Akiba C, Tew WP, Validation of a prediction tool for chemotherapy toxicity in older adults with cancer. J. Clin. Oncol. 34, 2366–2371 (2016). [PubMed: 27185838]
39. Kells AP, Fong DM, Dragunow M, During MJ, Young D, Connor B, AAV-mediated gene delivery of BDNF or GDNF is neuroprotective in a model of Huntington disease. Mol. Ther. 9, 682–688 (2004). [PubMed: 15120329]
40. Spencer KC, Sy JC, Ramadi KB, Graybiel AM, Langer R, Cima MJ, Characterization of mechanically matched hydrogel coatings to improve the biocompatibility of neural implants. Sci. Rep. 7, 1952 (2017). [PubMed: 28512291]
41. Dagdeviren C, Yang BD, Su Y, Tran PL, Joe P, Anderson E, Xia J, Doraiswamy V, Dehdashti B, Poston R, Khalpey Z, Ghaffari R, Huang Y, Slepian MJ, Rogers JA, Conformal piezoelectric energy harvesting and storage from motions of the heart, lung and diaphragm. Proc. Natl. Acad. Sci. U.S.A. 111, 1927–1932 (2014). [PubMed: 24449853]
42. Parastarfeizabadi M, Kouzani AZ, Advances in closed-loop deep brain stimulation devices. J. Neuroeng. Rehabil. 14, 79 (2017). [PubMed: 28800738]
43. Carrette S, Boon P, Sprengers M, Vonck K, Raedt R, Closed loop neurostimulation for epilepsy. Clin. Neurophysiol. 127, e40 (2016).
44. Rosin B, Slovik M, Mitelman R, Rivlin-Etzion M, Haber SN, Israel Z, Vaadia E, Bergman, Closed-loop deep brain stimulation is superior in ameliorating parkinsonism. Neuron 72, 370–384 (2011). [PubMed: 22017994]

45. Dagdeviren C, Shi Y, Joe P, Ghaffari R, Balooch G, Usgaonkar K, Gur O, Tran PL, Crosby JG, Meyer M, Su Y, Webb RC, Tedesco AS, Slepian MJ, Huang Y, Rogers JA, Conformal piezoelectric systems for clinical and experimental characterization of soft tissue biomechanics. Nat. Mater. 14, 728–736 (2015). [PubMed: 25985458]

46. Dagdeviren C, Su Y, Joe P, Yona R, Liu Y, Kim Y-S, Damadoran AR, Huang YA, Xia J, Martin LW, Huang Y, Rogers JA, Conformable amplified lead zirconate titanate sensors with enhanced piezoelectric response for cutaneous pressure monitoring. Nat. Commun. 5, 4496 (2014). [PubMed: 25092496]

47. Dagdeviren C, Joe P, Tuzman OL, Park K-I, Lee KJ, Huang Y, Rogers JA, Recent progress in flexible and stretchable piezoelectric devices for mechanical energy harvesting, sensing and actuation. ExtremeMech. Lett. 9, 269–281 (2016).

48. Rao PN, Kunzru D, Fabrication of microchannels on stainless steel by wet chemical etching. J. Micromech. Microeng. 17, N99–N106 (2007).

49. Chen Z-J, Gillies GT, Broaddus WC, Prabhu SS, Filmore H, Mitchell RM, Corwin FD, Fatourus PP, A realistic brain tissue phantom for intraparenchymal infusion studies. J. Neurosurg. 101, 314–322 (2004). [PubMed: 15309925]

50. Potter KA, Simon JS, Velagapudi B, Capadona JR, Reduction of autofluorescence at the microeletrode-cortical tissue interface improves antibody detection. J. Neurosci. Methods 203, 96–105 (2012). [PubMed: 21978484]

51. Kohane DS, Holmes GL, Chau Y, Zurakowski D, Langer R, Cha BH, Effectiveness of muscimol-containing microparticles against pilocarpine-induced focal seizures. Epilepsia 43 1462–1468 (2002). [PubMed: 12460246]

52. Feingold J, Desrochers TM, Fujii N, Harlan R, Tierney PL, Shimazu H, Amemori K.-i., Graybiel AM, A system for recording neural activity chronically and simultaneously from multiple cortical and subcortical regions in nonhuman primates. J. Neurophysiol. 107, 1979–1995 (2012). [PubMed: 22170970]

53. Feingold J, Gibson DJ, DePasquale B, Graybiel AM, Bursts of beta oscillation differentiate postperformance activity in the striatum and motor cortex of monkeys performing movement tasks. Proc. Natl. Acad. Sci. U.S.A. 112, 13687–13692 (2015). [PubMed: 26460033]

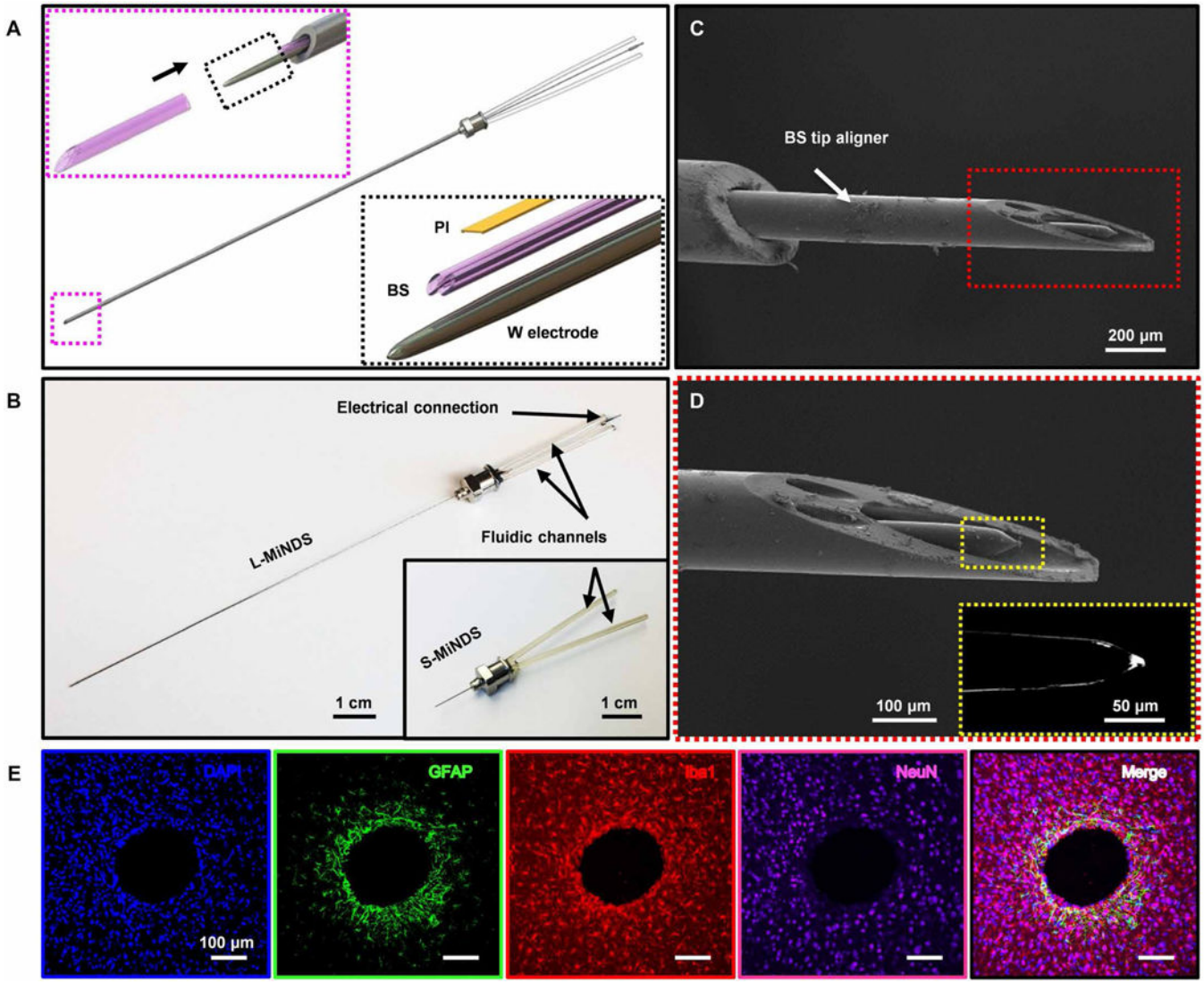

Fig. 1. A miniaturized neural drug delivery system: The MiNDS.

(**A**) Schematic illustration of a miniaturized neural drug delivery system (MiNDS) with an exploded view of the key device components (right, bottom inset) and with a magnified view of the borosilicate (BS) aligner tip aligning with the key device components in black arrow direction (left, top inset). (**B**) Image of L-MiNDS and S-MiNDS; electrical connection [tungsten (W) electrode] and the fluidic channels [borosilicate (BS)] are indicated. (**C**) Scanning electron microscopy (SEM) of the tip of L-MiNDS. (**D**) Magnified view of a BS aligner tip in the red dashed box in (C). The right inset shows the magnified view of W electrode in the yellow dashed box. (**E**) Representative confocal fluorescence images of horizontal brain slices showing the stab wound created by implanted MiNDSs, 8 weeks after implantation (n = 5 rats). Immunohistochemical staining for DNA (4′,6-diamidino-2-phenylindole, blue), astrocytes [glial fibrillary acidic protein (GFAP), green], microglia [ionized calcium binding adaptor molecule 1 (Iba1), red], neurons (NeuN, purple), and the merged signals are shown. Results are normalized to intensities 900 to 1100 μm away and averaged into 50-μm bins. The calculated error bars are the SDs.

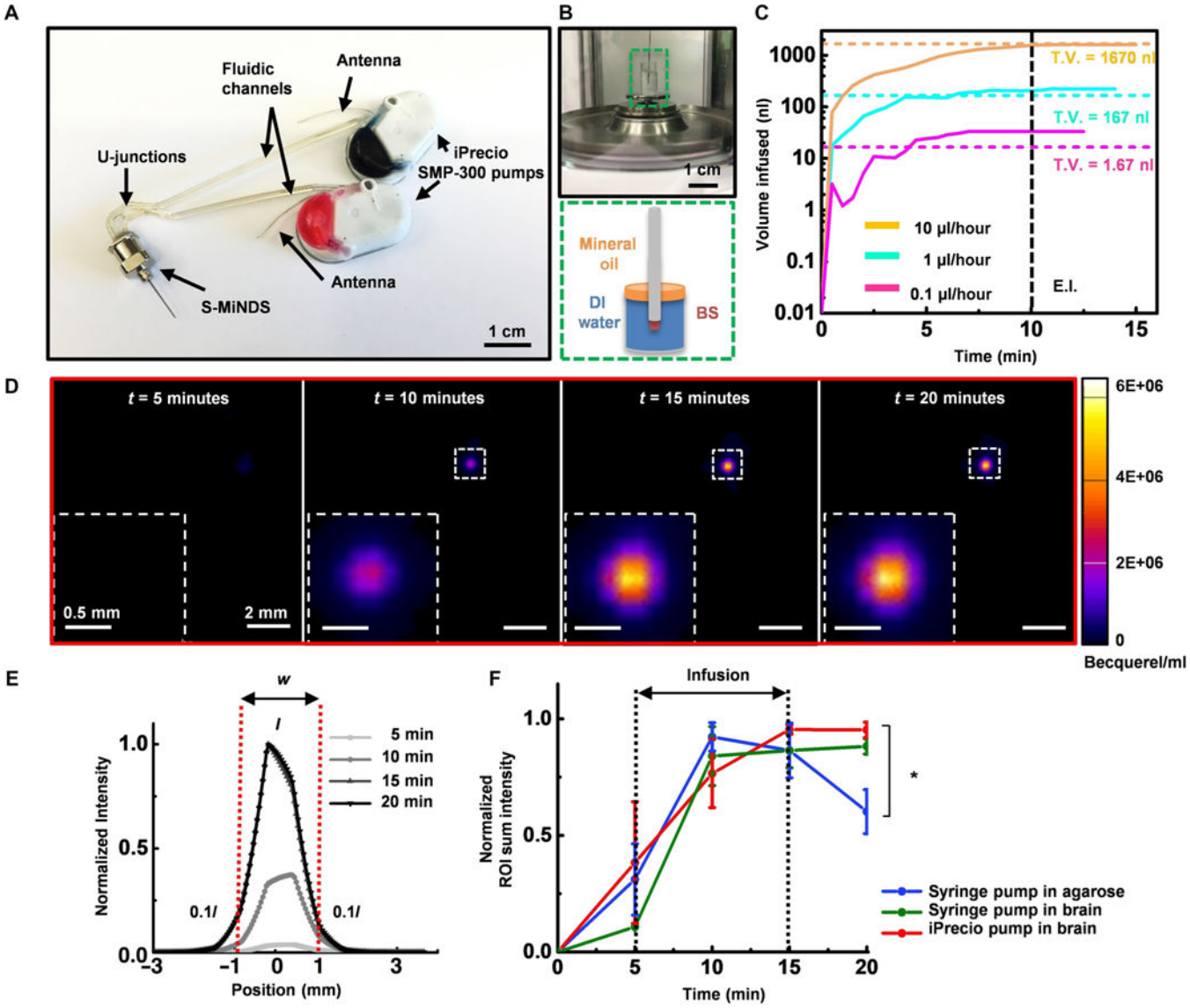

Fig. 2. In vitro and in vivo functionality of the S-MiNDS.

(**A**) Image of a MiNDS with U-junctions connected to two independently controlled iPrecio SMP-300 pumps. (**B**) Illustration of in vitro pump characterization setup with distinct layers of water and oil in the weighing dish as represented in green dashed box. (**C**) Line graph showing the mean infusion profiles of three infusion trials through S-MiNDS with flow rates 0.1, 1, and 10 µl/hour. End infusion (E.I.) (black dashed line) represents the end of infusion, and total volume (T.V.) (colored dashed lines) denotes the theoretical value of the volume infused. (**D**) Positron emission tomography (PET) images of Cu-64 in vivo delivery via an implanted MiNDS as seen in (A) (3 µCi/µl iPrecio infusion, 1.67-µl infusion at 10 µl/hour). Representative images at 5, 10, 15, and 20 min after Cu-64 injection show Cu-64 expression (fluorescence scale is depicted on the right). (**E**) Normalized fluorescence intensity in relation to position across the bolus. The diameter (*w*) of the bolus was determined using a three-dimensional (3D) region of interest (ROI), where the borders were defined as 10% of peak core intensity (*I*). (**F**) Normalized ROI sum fluorescence intensity at different times for

identical Cu-64 infusions delivered into an agarose phantom (0.6% by weight) and in the rat brain through implanted S-MiNDSs using a syringe pump and an iPrecio pump ($n = 3$ trials; error bars represent SE). Statistical analysis was done using one-way ANOVA followed by Tukey post hoc test at each time point. Significance differences were only found at time = 20 min. $*P < 0.05$. DI, deionized.

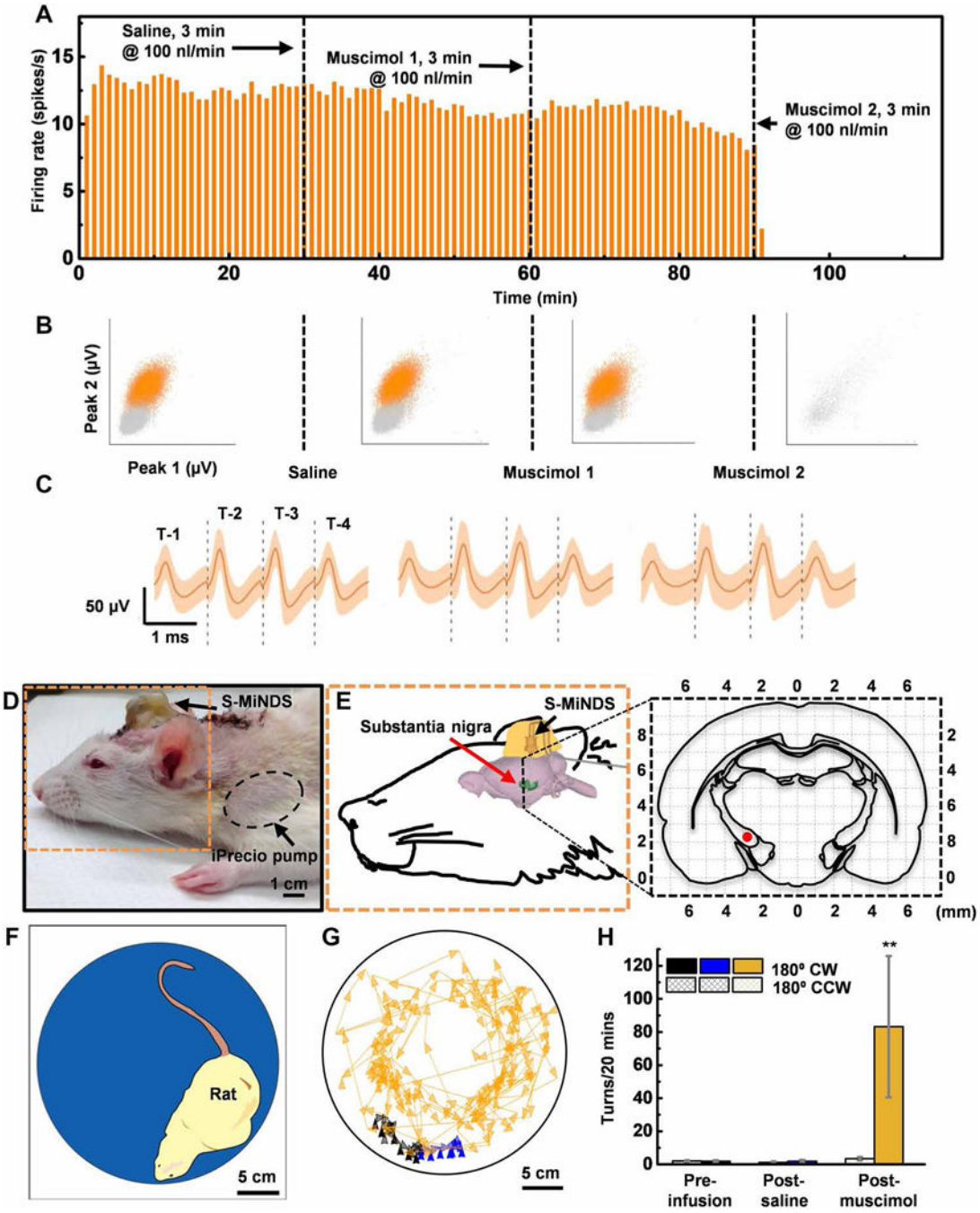

Fig. 3. Tetrode trials and behavioral study in rats.

(**A**) Firing rate histograms for 1-min bins of the recorded unit. The vertical black dashed lines indicate the start of saline infusion (first line at 30 min), the muscimol infusion (second line at 60 min), and the second muscimol infusion (third line at 90 min), respectively ($n = 1$). (**B**) Representations of sorted (orange) and unsorted (gray) action potentials based on peak values. Peaks 1 and 2 are the maximal value of waveforms measured by T-1 and T-2, respectively, during each period (preinfusion baseline, 22,928 waveforms; saline infusion, 20,940 waveforms; muscimol 1 infusion, 19,073 waveforms; and muscimol 2 infusion, 132

waveforms; $n = 1$ unit). (**C**) Averaged action potentials of a well-isolated unit (single unit) during each period (saline infusion, 20,940 wave-forms; muscimol 1 infusion, 19,073 waveforms; and muscimol 2 infusion, 132 waveforms; $n = 1$ unit). Orange shading represents a band around the mean with a width of three SDs. (**D** and **E**) Picture and schematic illustration (orange dashed outline) of a rat with an implanted MiNDS targeting substantia nigra. Expanded view of black dashed line in (E) shows coronal cross section of the brain 5-mm posterior to the bregma. The red dot identifies the position of the MiNDS tip within substantia nigra. (**F**) Schematic of a rat inside an opaque chamber during the behavioral study. (**G**) Color-tracking map of a rat during the preinfusion, post-saline, and post-muscimol infusions periods. (**H**) Mean number of 180° clockwise (CW) and counterclockwise (CCW) turns during preinfusion, post-saline, and post-muscimol infusion periods ($n = 3$ rats, 2 trials per rat; error bars represent SE; $^{**}P < 0.0021$). Statistical analysis was done using one-way ANOVA followed by Tukey post hoc test.

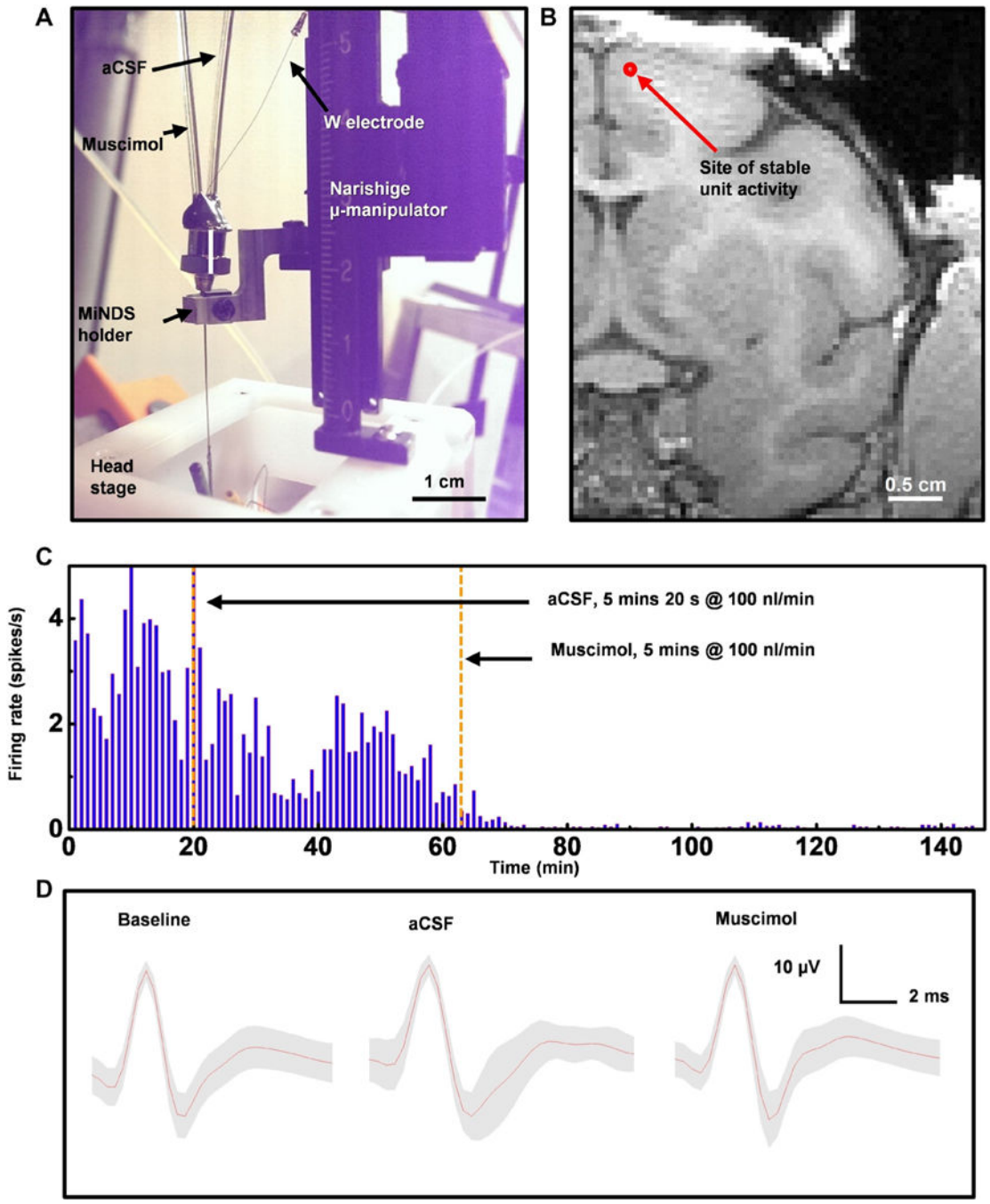

Fig. 4. In vivo MiNDS evaluation in an NHP.

(**A**) Image of an experimental setup integrated with the head stage of a nonhuman primate (NHP). (**B**) Magnetic resonance imaging (MRI) image showing the estimated location of the L-MiNDS infusion and recording. Estimated coordinates of the L-MiNDS tip are 22 mm (anteroposterior) and 2 mm (mediolateral) from the bregma. (**C**) Unit rate histograms for 1-min bins. The first vertical orange dashed line indicates the start of artificial cerebrospinal fluid (aCSF) infusion (at 20 min), and the second vertical orange dashed line denotes the time of muscimol infusion (at 63.7 min) (n = 1 unit). (**D**) Average waveforms for units

binned during each period (preinfusion baseline, 4593 waveforms; aCSF infusion, 51 waveforms; and muscimol infusion, 165 waveforms) with SD in gray shading